Flexural behaviour of stainless steel oval hollow sections

M. Theofanous, T. M. Chan and L. Gardner

Abstract

Structural hollow sections are predominantly square, rectangular or circular in profile. While square and circular hollow sections are often the most effective in resisting axial loads, rectangular hollow sections, with greater stiffness about one principal axis than the other, are generally more suitable in bending. Oval or elliptical hollow sections combine the aesthetic external profile of circular hollow sections with the suitability for resisting flexure of rectangular sections, whilst also retaining the inherent tosrional stiffness offered by all tubular sections. This paper examines the structural response of recently introduced stainless steel OHS in bending and presents design recommendations. In-plane bending tests in the three-point configuration about both the major and minor axis were conducted. All tested specimens were cold-formed from Grade 1.4401 stainless steel and had an aspect ratio of approximately 1.5. The full moment-rotation responses of the specimens were recorded and have been presented herein. The tests were replicated numerically by means of non-linear FE analysis and parametric studies were performed to investigate the influence of key parameters, such as the aspect ratio and the cross-section slenderness, on the flexural response. Based on both the experimental and numerical results, structural design recommendations for stainless steel OHS in bending in accordance with Eurocode 3: Part 1.4 have been made.

1. Introduction

The traditional family of structural hollow sections comprises square, rectangular and circular hollow sections. The general choice of section for carrying predominantly axial loading is either square or circular, while when bending is introduced, a rectangular section will generally be more efficient. The natural counterpart to a rectangular hollow section, but with a smooth external profile is an oval or elliptical hollow section. Hot-rolled carbon steel elliptical hollow sections (EHS) and cold-formed stainless steel oval hollow sections (OHS) have been recently introduced as tubular construction products. The flexural behaviour of such sections formed in stainless steel is the subject of the present study.

Previous research into the structural response of oval and elliptical hollow sections has included analytical and numerical investigations of elastic buckling and post-buckling [1-3], experimentation and derivation of slenderness limits [4-6] and examination of shear [7] and flexural buckling [8] behaviour. The resistances of EHS under combined loading [9] and with concrete infill [10-12] have also been studied, as have a range of EHS connection types [13-15]. On the basis of these studies, design rules for carbon steel EHS, principally in line with the provisions of Eurocode 3: Part 1.1 [16], have been developed. With regard to the structural behaviour of stainless steel OHS, efficient design rules in line with Eurocode 3: Part 1.4 [17] are sought. Experimental and numerical results on stainless steel OHS stub and long columns, together with appropriate design recommendations have been presented by the authors in a prior study [18]. The present paper focuses on the flexural response of stainless steel OHS, though comparisons are also made with the experimental results from previous studies on carbon steel EHS [6] and stainless steel CHS [19-21].

2. Experimental study

A laboratory testing programme was carried out to investigate the flexural response of stainless steel OHS in bending. A total of six beam tests in a three-point bending configuration was conducted with the principal aim of generating data that could be employed

in the determination of suitable slenderness parameters and cross-section classification limits. These tests were supplemented by six tensile coupon tests and six stub column tests, to obtain the basic material stress-strain response in both tension and compression. A detailed account of the tensile coupon tests and stub column tests is given in [18], whilst a summary of the determined material properties is given in Tables 1 and 2, respectively, of the present paper. The symbols E, $\sigma_{0.2}$, $\sigma_{1.0}$, σ_u, ε_f, n and $n'_{0.2,1.0}$ used in Tables 1 and 2 refer to Young's modulus, 0.2% proof stress, 1% proof stress, ultimate tensile stress, strain at fracture, Ramberg-Osgood strain-hardening parameters [22] below and above the 0.2% proof stress, respectively. These results are subsequently utilised during the analysis of the three-point bending tests and in the development of numerical models.

All tested material was austenitic stainless steel, grade 1.4401 (316), which contains approximately 18% chromium and 10% nickel [23]. All specimens were manufactured by Oval 316 as cold-rolled and seam welded sections with a minimum specified yield strength (0.2% proof strength) of 240 N/mm^2 according to EN 10088-2 [24]. However, the strength of cold-formed stainless steel sections is often far higher than both the minimum specified values and the mill certificate values for the flat sheet material, as a result of cold-work during forming [25-27].

Three section sizes – OHS 121×76×2, OHS 121×76×3 and OHS 86×58×3– were employed in the three-point bending tests to encompass a variety of section slenderness values and cover a range of structural responses. One major and one minor axis bending test was conducted for each section size. The specimens were cut to the required length using a rotary hacksaw and measurements of their geometry were taken prior to testing. Strain visualisation grids were marked onto the specimens at a spacing of 20 mm.

Initial geometric imperfections were measured to aid in the assessment of the structural behaviour of the beams and in the development of the numerical models. Due to the high tosrional stiffness brought about by the closed shape of the OHS, lateral-tosrional buckling was not an issue for the span lengths considered in this study and hence global imperfections were not examined. Measurements of local imperfections were conducted following procedures from similar previous studies [18, 28]. The specimens were firstly secured to the flat bed of a milling machine. Subsequently, a displacement transducer was attached to the head of the milling machine and a manual feed was used to pass the specimen under the

transducer. Readings were taken at 20 mm intervals along the centrelines of both the minor and major axes of the specimens. The datum line for the imperfection measurements was initially taken as a straight line spanning between the ends of each specimen's face. However, it was observed that the release of residual stresses following cutting to length induced flaring at the ends of the specimens, thereby significantly magnifying the measured imperfection amplitudes, but these were not representative of the general geometric imperfection pattern along the length of the specimens. Furthermore, the imperfection pattern at the ends of the simple beam specimens tested herein has little influence on their flexural response, since the maximum moment arises at mid-span and hence this is where local imperfections are of greatest importance. The effect of the end flaring was therefore removed by considering only the middle 50% of the specimens' length in the definition of the datum line, as proposed in [29].

Based on the measured geometry, an equation of an ellipse was fitted to the mid-surface of the specimens, which was found to accurately represent the actual geometry as can be seen in Fig. 1. The relevant section moduli (i.e. $W_{el,y}$, $W_{el,z}$, $W_{pl,y}$ and $W_{pl,z}$) were calculated by assuming the OHS to have a constant thickness (which was verified by the measurements taken) and numerically integrating along the mid-surface of the ellipse, in accordance with [6]. The notation regarding the cross-sectional geometry used throughout the paper is depicted in Fig. 2, whilst all measured geometric data, the section moduli for the relevant axis of bending and the maximum measured initial imperfection amplitudes are summarised in Table 3. The designation of the specimens adopted in the present study includes the section type (OHS), the nominal major and minor axis outer dimensions, the nominal thickness and the axis of bending (MA for major and MI for minor axis bending).

The beams were simply supported between rollers, which were placed 50 mm inward from each end of the beam as depicted in Fig. 3. Steel collars (25 mm in width) machined to the profiles of the oval sections, were employed at the points of load introduction and support. Profiled wooden blocks with a width of 25 mm were inserted in the tubes at the loading point and at the support points to prevent local bearing failure. A linearly varying displacement transducer (LVDT) was placed at mid-span to measure the mid-span vertical deflection, whilst two additional LVDTs were positioned at each end of the specimens in order to determine the rotation of the beams at the support points, as shown in Fig. 3. Strain gauges were also attached to each beam at a distance of 50 mm from the mid-span to measure the

strain at the extreme tensile and compressive fibres of the cross-sections. Load, strain, displacement, and input voltage were all recorded at 2 second intervals using the data acquisition system DATASCAN.

Load was applied at mid-span using a 50 T Instron hydraulic actuator, which was connected to a load cell and controlled through an Instron control cabinet. Displacement control was utilized in order to capture the full moment-rotation response, including into the post-ultimate region. The obtained moment-rotation curves are depicted in Figs. 4 and 5 for the major and minor axis bending specimens respectively. It should be noted that the reported rotation refers to the total rotation at mid-span (location of the idealised plastic hinge), which is calculated as the sum of the measured end rotations, whilst the applied bending moment was calculated directly from the applied force. For comparison purposes, all curves have also been plotted in non-dimensional form in Fig. 6, where for each section the applied moment has been normalised by the respective plastic moment capacity M_{pl} (calculated as the plastic modulus W_{pl} multiplied by the tensile 0.2% proof strength $\sigma_{0.2}$ given in Table 1), whilst the corresponding total rotation at mid-span has been normalised by the elastic component of the total rotation corresponding to M_{pl}, defined as θ_{pl} and given by Eq. (1):

$$\theta_{pl} = \frac{M_{pl}L}{2EI} \tag{1}$$

where L is the span between the supports, E is Young's modulus as obtained from the tensile coupon tests and I is the second moment of area for the appropriate axis of bending as calculated by means of numerical integration.

All six specimens displayed evidence of ovalization (reduction of the section's height due to flattening in the plane of bending) outside the region of the central collar at high strains. Similar observations have been reported for CHS in bending in previous studies [30, 31]. The beams ultimately failed by inelastic local buckling of the compression (upper) portion of the sections in the region of maximum moment near the point of loading (See Fig. 7). For specimens tested about their minor axis, local buckling initiated at the point of greatest radius of curvature (i.e. the flattest part of the section), which coincided with the point of maximum compressive stress. For specimens tested in major axis bending local buckling initiated near the extreme compressive fibre though deformations spread further down the section towards

the neutral axis. This pattern of local buckling may be expected since, in major axis bending, although the compressive stress is reducing towards the neutral axis, the local stiffness of the section (which is strongly influenced by the local curvature) is also reducing.

All key experimental results are summarised in Table 4. The elastic and plastic moment capacities, M_{el} and M_{pl} were evaluated by multiplying the relevant section modulus (W_{el} or W_{pl} given in Table 3) by the measured tensile 0.2% proof strength $\sigma_{0.2}$, whilst the rotation capacities R were evaluated using Eq. (2):

$$R = \frac{\theta_u}{\theta_{pl}} - 1 \tag{2}$$

where θ_{pl} is the elastic component of the rotation when M_{pl} is reached as defined by Eq. (1) and θ_u refers to the total rotation at mid-span when the moment-rotation curve falls back below M_{pl} and is obtained from the test results. All test results together with the numerical results generated from subsequent parametric studies are discussed in detail in Section 4.

3 Numerical modelling

Numerical simulations were performed in parallel with the experimental studies. The finite element (FE) package ABAQUS [32] was employed to replicate the experimental results and assess the sensitivity of the numerical models to key parameters such as initial geometric imperfections, material properties and mesh density. Upon validation of the numerical models, parametric studies were conducted to expand the available structural performance data over a wider range of cross-sectional slendernesses and aspect ratios and thus to investigate the effect of these key parameters on the flexural response of stainless steel OHS.

As successfully employed in similar previous studies [2, 5, 6, 8, 18], the reduced integration 4-noded doubly curved general-purpose shell element S4R with finite membrane strains [32] has been employed in the present study. In order to minimize computational time while still generating accurate results, a mesh convergence study based on elastic eigenvalue buckling analyses was carried out. A uniform mesh size along both the circumference and length of the

models of size 2a/10(a/b)×2a/10(a/b) (where a and b are defined in Fig. 2) was chosen. The same mesh size was deemed suitable in similar modelling applications for both carbon steel EHS [5, 6] and stainless steel OHS [18].

All failure modes observed during testing were symmetric with respect to the plane of bending. In order to further reduce computational time, only one half of each section was modelled and suitable symmetry boundary conditions were applied along the plane of bending. The effect of the steel collars and wooden blocks located at the supports and at mid-span was taken into account in the FE simulations by ensuring that the respective cross-sections remained undeformed at these locations, using kinematic coupling. Results were found to be insensitive to whether a single cross-section (i.e. one line of nodes) or a 25 mm length of beam (corresponding to the width of the collar and wooden block) were restrained; thus the former approach was employed at the loading point and supports. Simple support conditions were simulated by restraining suitable degrees of freedom at the ends of the beams. The beam was restrained longitudinally at one end only.

Measured geometry and material properties as obtained from testing were incorporated into the models. The adopted material model is a compound Ramberg-Osgood [33, 34] formulation, with the second stage of the model utilising the 1.0% proof stress $\sigma_{1.0}$. Two-stage material models for stainless steel have been developed and studied by a number of authors [22, 35-38]. The material parameters given in Tables 1 and 2 were averaged for each nominal cross-section size and applied uniformly to each model in the true stress σ_{true} - log plastic strain ε_{ln}^{pl} format, as required by ABAQUS [32] and defined by Eqs. (3) and (4):

$$\sigma_{true} = \sigma_{nom}(1 + \varepsilon_{nom}) \tag{3}$$

$$\varepsilon_{ln}^{pl} = \ln(1 + \varepsilon_{nom}) - \frac{\sigma_{true}}{E} \tag{4}$$

where σ_{nom} and ε_{nom} are the engineering stress and strain respectively and E is the Young's modulus.

Regarding the incorporation of the material model into the FE simulations, another issue arises since a piecewise linear approximation of the actual continuous engineering stress-strain curve has to be derived, which can be thereafter converted into the desired format using Eqs. (3) and (4). An optimized distribution of the approximation points, which maximises the accuracy of the fit for a given number of discretisations, is pursued. In a similar investigation [39], it was concluded that the density of the points defining the multilinear curve should be proportional to the curvature of the Ramberg-Osgood model. This approach has been followed in the present study, with a slight modification since a compound Ramberg-Osgood curve rather than the original single expression is used. The engineering stress-strain curve was initially divided into two regions; the first one being limited by the 0.2% proof stress $\sigma_{0.2}$, whilst the second one being limited by the ultimate tensile stress σ_u. From the number of points to be used for the discretisation of the stress-strain curve, three are reserved for the representation of the origin and the end of the curve as well as the point corresponding to $\sigma_{0.2}$, whilst the remaining points are then divided between the first and the second region in proportion to the $\dfrac{\sigma_{0.2}}{\sigma_u - \sigma_{0.2}}$ ratio. Finally, the points to be used in each region are distributed so that their density is proportional to the curvature of each sub-curve comprising the whole material response.

Residual stresses were not measured in the experimental part of this study. However, the presence of residual stresses is implicitly reflected in the material properties obtained from both tensile coupon and stub column tests. For tensile coupons, provided they are not straightened by plastic deformation prior to testing, the measured stress-strain response will inherently include the effect of bending residual stresses, since these are approximately reintroduced during gripping and upon the application of light loads [40, 41]. The material properties obtained from stub columns include the presence of both membrane and bending residual stresses, though their influence will vary under different loading conditions. Residual stresses were therefore not explicitly included in the numerical models in this investigation; a similar approach has been successfully followed in previous studies [18, 42].

During production, fabrication and handling of structural members, geometric imperfections (i.e. deviations of the actual member geometry from the idealised one) are generated, which may significantly affect the structural response. Owing to the absence of member buckling, only local geometric imperfections were considered in the numerical models. These were

incorporated in the form of the lowest buckling mode shape, as obtained from linear eigenvalue buckling analyses. For each model, two analyses were carried out; a linear eigenvalue buckling analysis employing the subspace iteration method [32] for eigenmode extraction was initially conducted and the lowest buckling mode shape obtained was incorporated into a subsequent geometrically and materially non-linear analysis as a representation of the local geometric imperfections. For the non-linear analysis, the modified Riks method [32] was utilised, in order to trace the full moment-rotation response of the models, including into the post-ultimate (i.e. falling branch) region. The imperfection amplitude was varied to assess the sensitivity of the models and four cases were considered: the maximum measured imperfection as given in Table 3, zero imperfection and two fractions of the cross-sectional thickness, namely t/10 and t/100.

Initial imperfection amplitude and material properties were found to be the key features affecting the models' response. Incorporation of tensile material properties resulted in marginal overpredictions of the ultimate moment observed in the corresponding tests, whilst the use of compressive material properties (as derived from stub column tests) improved the predictions in terms of strength but did not improve the accuracy in terms of rotations. The closest agreement between test and FE results was obtained when the stub column properties were assigned to the part of the model in compression and the tensile properties were assigned to the part that was stressed in tension. This approach was therefore followed throughout the numerical study. The effect of the imperfection amplitude on the response can be assessed from Table 5 where the comparison between bending test results and FE results for varying local imperfection amplitudes is displayed. It can be seen that accurate results in terms of moment capacity are obtained for all considered imperfection amplitudes, whereas the rotation capacity R was found to be more sensitive to imperfections. As in the tests, ovalization of the specimens was evident in the geometrically and materially non-linear FE analyses. This ovalization resulted in a decrease in flexural rigidity of the beams and promoted the onset of local buckling even in the case where no initial local imperfection was incorporated into the non-linear analysis. Approaching ultimate moment, the magnitude of the additional imperfection caused by ovalization overshadowed the initial geometric imperfection amplitude incorporated in the models. Therefore, the response of the models, particularly in terms of maximum attained moment, was relatively insensitive to the prescribed initial imperfection amplitudes.

In general, the FE models displayed good agreement with the experimental results and were capable of replicating the experimentally observed structural response of the specimens. Best agreement in terms of both peak moments and rotations was obtained for an initial imperfection amplitude of t/10, as shown in Table 5. In all cases, experimental and numerical failure modes were similar, as indicated in Figs. 8 and 9. The full moment-rotation response, including initial stiffness, peak moment and post-ultimate response was generally well predicted by the FE simulations, as displayed in Figs. 10 and 11 where the numerical moment-rotation curves for OHS 121×76×3-MI and OHS 86×58×3-MA are compared with the respective experimental curves. The initial elastic stiffness is included in both figures for comparison purposes.

Having validated the numerical models against the experimental results, parametric studies were carried out to investigate the behaviour of stainless steel OHS in bending over a wider range of cross-section slenderness in order to derive suitable slenderness limits. Both major and minor axis bending were studied. Local imperfections assumed the pattern of the elastic lowest buckling mode shape with an amplitude of t/10, whilst the material properties of OHS 121×76×3 were incorporated in the models (tensile material properties for the lower (tension) part of the beam and stub column properties for the upper (compression) part). Two aspect ratios, 1.5 (corresponding to currently available stainless steel OHS) and 2 (corresponding to the current range of carbon steel EHS), were considered. All modelled cross-sections had a larger outer diameter of 120 mm and a length of 1000 mm, whilst the smaller diameter was set to either 80 mm or 60 mm to achieve an aspect ratio of 1.5 or 2 respectively. The thickness of the models was varied between 0.4 mm and 8.9 mm for the OHS 120×80 sections and between 0.6 mm and 11.8 mm for the 120×60 sections, thereby covering a slenderness range $D_e/t\varepsilon^2$ (described in Section 4) between 40 and 320 for both major and minor axis bending. The obtained results are discussed in Section 4, where comparisons with carbon steel EHS and stainless steel CHS are also displayed.

4 Analysis of results

4.1 Cross-section classification

Most modern structural steel design codes, including Eurocode 3: Part 1.1 [16], employ the cross-section classification process for the treatment of local buckling of cross-sections subjected either partly or fully to compression. The concept of classification is based on an assumed bilinear stress-strain behaviour with a material specific and well-defined yield point, which imposes an upper limit (i.e. the yield strength) on the stress level that can be attained by a cross-section. Despite the absence of such a limit for stainless steel, due to the rounded nature of its material response [35-37, 43], the same approach is followed by Eurocode 3: Part 1.4 [17] for the treatment of local buckling in stainless steel elements, so that consistency between carbon steel and stainless steel design is maintained.

Within the cross-section classification framework, cross-sections are assigned to discrete behavioural classes (for a given loading case) according to their susceptibility to local buckling as estimated by comparing a suitable slenderness parameter to codified slenderness limits. These limits depend on stress distribution, boundary conditions and material properties. Cross-sections that are prone to local buckling before the attainment of their elastic moment capacity are characterised as slender (Class 4), whereas they are classified as Class 3 if failure occurs beyond the elastic moment capacity M_{el} but below the plastic moment capacity M_{pl}. Cross-sections that are able to exceed their plastic moment capacity but have limited deformation capacity are assigned to Class 2, whilst they become Class 1 if they possess sufficient deformation capacity to be used in plastic design. The structural responses associated with these four behavioural groups are depicted in terms of moment-rotation characteristics in Fig. 12. The deformation capacity is defined in terms of rotations θ or curvatures k as shown in Fig. 13 and is quantified through Eq. (2). Plastic design of stainless steel structures is not currently permitted in Eurocode 3: Part 1.4, despite the provision of a Class 1 slenderness limit. For consistency, the rotation capacity requirement for Class 1 carbon steel section, R=3 [44, 45], is adopted in the present study.

In the following subsections, suitable slenderness parameters for stainless steel OHS subjected to bending about their major and minor axes are proposed and the codified slenderness limits for stainless steel and carbon steel CHS in bending are assessed, based on

both experimental and numerical results. In all code comparisons presented in this section, the experimentally obtained tensile material properties and measured geometry have been used, with all safety factors set to unity.

4.2 Slenderness parameters

The definition of suitable slenderness parameters is crucial for the classification of any cross-section. For cross-sections comprising flat plated elements, each constituent plate element is individually classified based on its width-to-thickness (b/t) ratio independently of the other constituent elements; the whole cross-section is classified by its most slender (least favourably classified) constituent element. For CHS, the diameter-to-thickness (D/t) ratio is employed as a suitable slenderness parameter. In both cases, the local radius of curvature and hence the local stiffness associated with the element (for plated cross-sections), or cross-section (for CHS) considered, are constant (i.e. ∞ for a plate and D/2 for CHS). For OHS and EHS the local radius of curvature changes around the cross-section as described by Eq. (5) where φ is defined in Fig. 2. The local radius of curvature assumes its maximum value $r_{max}=a^2/b$ at $\varphi=0$, which is therefore the least stiff region of the cross-section, and its minimum value $r_{min}=b^2/a$ at $\varphi=\pi/2$, which is therefore the stiffest region of the cross-section.

$$r = \frac{b^2}{a}\left(\sin^2\varphi + \frac{a^2}{b^2}\cos^2\varphi\right)^{3/2} \tag{5}$$

As discussed earlier, for minor axis bending, local buckling initiates at the point of greatest radius of curvature which coincides with the most heavily compressed part of the cross-section. The same is true for OHS stub columns under uniform compression. Therefore the slenderness parameter proposed for OHS in axial compression [18] is adopted for minor axis bending of OHS in the current study. A similar approach was followed for carbon steel EHS in [4, 6]. The proposed slenderness parameter is defined by Eq. (6):

$$\frac{D_e}{t\varepsilon^2} = 2\frac{(a^2/b)}{t\varepsilon^2} \tag{6}$$

where D_e is an equivalent diameter defined as two times the maximum radius of curvature in an elliptical section which is equal to $2(a^2/b)$ and $\varepsilon = \sqrt{\dfrac{235}{\sigma_{0.2}}\dfrac{E}{210000}}$ as specified in [17].

For major axis bending, local buckling initiates at a point of the cross-section between the neutral axis and the major axis, since the maximum compressive stress arises at the stiffest part of the cross-section. This issue has been addressed analytically and the location of initiation of local buckling in shells of varying curvature in bending was determined by Gerard and Becker in [46]. Based on these findings and experimental observations, Chan and Gardner [6] proposed the slenderness parameter defined by Eqs. (7) and (8) for major axis bending of carbon steel EHS, which are adopted for stainless steel OHS in the present study.

$$\frac{D_e}{t\varepsilon^2} = 0.8\frac{(a^2/b)}{t\varepsilon^2} \quad \text{for} \quad a/b > 1.357 \tag{7}$$

$$\frac{D_e}{t\varepsilon^2} = 2\frac{(b^2/a)}{t\varepsilon^2} \quad \text{for} \quad a/b \leq 1.357 \tag{8}$$

The threshold of 1.357 ensures continuity of the two branches defining the slenderness parameter. Its physical meaning is that for aspect ratios less than 1.357 local buckling initiates at the most heavily stressed part of the cross-section despite it also being the stiffest part, while for higher aspect ratios the point of initiation of local buckling moves from the extreme compression fibre towards the neutral axis.

4.3 Class 3 limit

Cross-sections able to exceed their elastic moment capacity are classified as Class 3 or better. The M_u/M_{el} (ultimate moment over elastic moment capacity) ratios of all experimental and FE data on stainless steel OHS bending about their minor axis have been plotted against the relevant cross-section slenderness parameter defined by Eq. (6) in Fig. 14; stainless steel CHS [19-21] and carbon steel EHS [6] minor axis test data have been included for comparison purposes. The respective major axis data plotted against the cross-section slenderness defined by Eq. (7) are depicted in Fig. 15, where the relevant stainless steel CHS and carbon steel EHS have also been included. It should be noted that in the stocky region of the graphs, the curves derived from parametric studies display slightly higher moment capacities than the test

results obtained for OHS 86×58×3. This is due to the different strain hardening characteristics inherent in the material properties of OHS 121×76×3 upon which the parametric studies based; a summary of material properties is given in Tables 1 and 2.

It should be noted that all depicted CHS test data have been obtained from 4-point bending tests, whereas all OHS data (both experimental and numerical) have been derived from 3-point bending tests. Carbon steel EHS have been tested in both 3-point and 4-point bending configurations and the respective test points are assigned a different symbol in Figs 14 and 15. The effect of moment gradient on ultimate moment and rotation capacity has been extensively studied in previous investigations [47-49] regarding carbon steel I sections. It has generally been concluded that both ultimate moment capacity and rotation capacity are improved in the presence of a moment gradient, as compared to uniform bending. The explanation for this relates to the level of restraint provided to the section in the region of local buckling - in 4-point bending, yielding (and the associated loss of stiffness) occurs throughout the zone of uniform moment, thus limited restraint is provided to any point of initiation of buckling. However, in 3-point bending arrangements, local buckling initiates at the most heavily loaded cross-section; material either side of this point is less heavily stressed due to the moment gradient and is thus able to provide greater restraint against local buckling.

Previous studies [47-49] have shown that the moment gradient has a more pronounced effect on rotation capacity than ultimate moment capacity, and the steeper the moment gradient the higher the rotation capacity. Ultimate moment resistance is generally less sensitive to moment gradient due to the yield plateau (with increasing deformation only resulting in small increments in load carrying capacity), though for stocky sections that reach the strain-hardening regime or for materials, such as cold-formed carbon steel and stainless steel, that exhibit a more rounded stress-strain response, increases in ultimate moment can be more significant. It can thus be asserted that for a given cross-section slenderness, a stainless steel member subjected to a moment gradient is expected to reach a higher ultimate moment and possess higher rotation capacity than it would under uniform moment.

In both Figs 14 and 15 the same general trend can be seen: the M_u/M_{el} ratio decreases with increasing cross-section slenderness and, for a given slenderness, performance improves with increasing aspect ratio. The stainless steel OHS test members and the curves derived from the parametric studies display higher moment capacities than their CHS counterparts of similar

slenderness. This is believed to relate to both their higher aspect ratio and to the moment gradient that they are subjected to. The stainless steel OHS perform similarly to the carbon steel EHS under 3-point bending, while the influence of varying moment gradient only can be seen by comparing the results of the carbon steel EHS in 3- and 4-point bending.

The codified Class 3 limits [16, 17] are also depicted in Figs 14 and 15. The stainless steel limit of $280\varepsilon^2$ is significantly more relaxed than the carbon steel limit of $90\varepsilon^2$, which appears overly conservative. A more relaxed Class 3 slenderness limit of $140\ \varepsilon^2$ has been previously proposed for both CHS and EHS in bending [6]. It is proposed herein that the current Class 3 limit for stainless steel CHS in bending of $280\varepsilon^2$ may also be applied to stainless steel OHS for both major and minor axis bending. Despite seeming overly conservative for OHS, it should be bourn in mind that the derivation of the stainless steel CHS limit was based on 4-point bending test data, whereas the depicted OHS FE curves are derived for a moment gradient. Hence the superior behaviour of the OHS cannot be attributed solely to the effect of the aspect ratio, but will also reflect the beneficial effect of the moment gradient.

4.4 Class 2 limit

Cross-sections capable of exceeding their plastic moment capacity are assigned to Class 2. Figs 16 and 17 depict the M_u/M_{pl} (ultimate moment over plastic moment capacity) ratios as a function of cross-section slenderness for all OHS test and FE data in minor and major axis bending respectively. The relevant carbon steel EHS and stainless steel CHS data are also included as before. Similarly to Figs 14 and 15, M_u/M_{pl} increases with decreasing slenderness. However the effect of aspect ratio is less pronounced in this case, with the FE curves derived for an aspect ratio of 1.5 and 2 lying very close to each other throughout the considered slenderness range.

Previous remarks regarding the effect of moment gradient and the relative performance of stainless steel OHS in comparison to stainless steel CHS and carbon steel EHS are also supported by Figs. 16 and 17. The common stainless steel and carbon steel Class 2 slenderness limit of $70\varepsilon^2$ is suitable for OHS in either major or minor axis bending.

4.5 Class 1 limit

As mentioned in Section 4.1, the rotation capacity requirement for plastic design of R=3 utilised for carbon steel [44, 45] is also adopted in the current study for stainless steel. Hence, all cross-section with a rotation capacity as defined in Eq. (2) equal to or greater than 3 are deemed to be Class 1 sections.

The rotation capacity R derived from the OHS test and numerical data from the present study, together with the existing EHS test data is plotted against the relevant slenderness parameter in Figs 18 and 19 for minor and major axis bending respectively. Stainless steel CHS data have also been included. Note that the carbon steel EHS subjected to 4-point bending, rotation capacity has been calculated on the basis of Eq. (9), where $k_{pl,0.95}$ is the elastic rotation at $0.95M_{pl}$ and $k_{rot,0.95}$ is the rotation at which the falling moment branch passes $0.95M_{pl}$ [6]. This approach has been applied in previous studies [6, 30] to overcome the problem that the results of 4-point bending tests often exhibit a bending moment plateau just below M_{pl} due to the formation of a plastic zone (in contrast to a more localised plastic hinge associated with a 3-point bending test arrangement) and possible ovalisation prior to the attainment of strain hardening. Adoption of Eq. (9) provides a more stable measure of rotation capacity that is comparable with that obtained from 3-point bending tests. For stainless steel, the continuous strain-hardening nature of the material counteracts these effects and the conventional definition of rotation capacity based on the full plastic moment capacity may be calculated through Eq. (2).

$$R_{0.95} = \frac{k_{rot,0.95}}{k_{pl,0.95}} - 1 \qquad (9)$$

In Fig. 18 it can be seen that aspect ratio is not a particularly influential factor in determining rotation capacity as the FE curves derived for aspect ratios of 1.5 and 2 follow a similar path throughout the slenderness range considered, though some deviation may be observed for stocky sections in major axis bending. The results indicate that the current Class 1 slenderness limit of $50\varepsilon^2$ common to both carbon steel and stainless steel may be safely applied to stainless steel OHS in major or minor axis bending.

4.6 Prediction of actual bending capacity

Given the rounded nature of stainless-steel's stress-strain curve and the absence of a sharply defined yield point, use of the conventional classification system and the definition of M_{el} and M_{pl} has been viewed as unduly restrictive since stresses beyond the 0.2% proof stress $\sigma_{0.2}$ (due to strain hardening) are not accounted for. This has been highlighted in previous studies investigating the ultimate capacity of stainless steel cross-sections and members and an alternative design method, termed the continuous strength method (CSM) has been developed [22, 37, 50] and statistically validated [51]. The CSM has also been applied successfully to structural carbon steel [52].

The CSM currently covers the design of stainless steel plated sections and CHS subjected to compression and bending. Its application to stainless steel OHS has been explored in the present study. The OHS were treated as CHS with an equivalent diameter equal to D_e as defined in Eqs. (6), (7) and (8) according to axis of bending and aspect ratio. On average, the ultimate moment is well-predicted with an average M_{CSM}/M_u (moment capacity obtained from the CSM over ultimate test moment) ratio of 0.90 and a coefficient of variation of 0.06. The respective Eurocode predictions have an average M_{EC3}/M_u (moment capacity obtained according to Eurocode 3: Part 1.4 [17] over ultimate test moment) ratio of 0.78 and a coefficient of variation of 0.12. Hence, application of the CSM leads to a 15% increase in efficiency and a 50% reduction in scatter of prediction.

5 Conclusions

Six in-plane 3-point bending tests on stainless steel oval hollow sections have been performed. Three section sizes with an aspect ratio of approximately 1.5 and varying cross-section slenderness were tested in major and minor axis bending. The tests were replicated by means of FE simulations and, upon validation of the FE models, parametric studies were conducted to examine the effect of key variables on moment resistance and rotation capacity. Previous studies on carbon steel EHS [2] in major and minor axis bending were utilised and the slenderness parameters originally proposed for carbon steel EHS were adopted in the present study. Both test and FE results were compared with existing test data on stainless steel CHS and carbon steel EHS and the effect of aspect ratio, cross-section slenderness and moment gradient on strength and deformation capacity has been highlighted. It was concluded

that current codified slenderness limits for stainless steel CHS may safely be adopted for stainless steel OHS in conjunction with proposed equivalent diameters D_e, whilst the actual moment capacity (allowing for strain-hardening) may be reliably predicted using the continuous strength method.

References

[1] Kempner J, Chen YN. (1968). Post-buckling of an axially compressed oval cylindrical shell. In: 12th International Congress of Applied Mechanics. Stanford University. 246-256.

[2] Ruiz-Teran, A. M. and Gardner, L. (2008). Elastic buckling of elliptical tubes. Thin-Walled Structures. 46(11), 1304-1318.

[3] Silvestre, N. (2008). Buckling behaviour of elliptical cylindrical shells and tubes under compression. International Journal of Solids and Structures. 45(16), 4427-4447.

[4] Gardner, L. and Chan, T. M. (2007). Cross-section classification of elliptical hollow sections. Steel and Composite Structures. 7(3), 185-200.

[5] Chan, T. M. and Gardner, L. (2008). Compressive resistance of hot-rolled elliptical hollow sections. Engineering structures, 30(2), 522-532.

[6] Chan, T.M. and Gardner, L. (2008). Bending strength of hot-rolled elliptical hollow sections. Journal of Constructional Steel Research, 64(9), 971-986.

[7] Gardner, L., Chan, T. M. and Wadee, M. A. (in press). Shear response of elliptical hollow sections. Proceedings of the Institution of Civil Engineers - Structures and Buildings.

[8] Chan, T.M. and Gardner, L. (in press). Flexural buckling of elliptical hollow section columns. Journal of Structural Engineering, ASCE.

[9] Nowzartash, F. and Mohareb, M. (submitted). Plastic Interaction Relations for Elliptical Hollow Sections. Thin-Walled Structures.

[10] Yang, H., Lam, D. and Gardner, L. (2008). Testing and analysis of concrete-filled elliptical hollow sections. Engineering Structures. 30(12), 3771-3781.

[11] Roufegarinejad, A., and Bradford, M. A. (2007). Local buckling of thin-walled elliptical tubes containing an elastic infill. Proceedings of the 3rd International Conference on Steel and Composite Structures, Manchester, United Kingdom, 943-948.

[12] Zhao, X. L., Lu, H. and Galteri, S. (2007). Tests of Elliptical Sections Filled with SCC (Self-Compacting Concrete). Proceedings of the 5th International Conference on Advances in Steel Structures. Singapore, 950-955.

[13] Martinez-Saucedo G., Packer J.A., Zhao X.L. (2008). Static design of elliptical hollow section end connections. Proceeding of the Institution of Civil Engineers-Structures and Buildings. 161(2), 103-113.

[14] Choo, Y. S., Liang, J. X., and Lim, L. V. (2003). Static strength of elliptical hollow section X-joint under brace compression. Proceedings of the 10th International Symposium on Tubular Structures, Madrid, Spain, 253-258.

[15] Willibald, S., Packer, J. A. and Martinez-Saucedo, G. (2006). Behaviour of gusset plate connections to ends of round and elliptical hollow structural section members. Canadian Journal of Civil Engineering, 33(4), 373-383.

[16] EN 1993-1-1. (2005) Eurocode 3: Design of steel structures - Part 1.1: General rules – General rules and rules for buildings. CEN.

[17] EN 1993-1-4. (2006) Eurocode 3: Design of steel structures - Part 1.4: General rules - Supplementary rules for stainless steel. CEN.

[18] Theofanous, M., Chan, T.M. and Gardner, L. (submitted). Structural response of stainless steel oval hollow sections compression members. Engineering Structures.

[19] ECSC (2000). Final Report. ECSC project – Development of the use of stainless steel in construction. Document RT810, Contract No. 7210 SA/ 842, The Steel Construction Institute, UK.

[20] Kiymaz, G. (2005). Strength and stability criteria for thin-walled stainless steel circular hollow section members under bending. Thin-Walled Structures. 43 (10), 1534-1549.

[21] Rasmussen, K.J.R. and Hancock, G.J. (1993). Design of cold-formed stainless steel tubular members II: Beams. Journal of Structural Engineering, ASCE, 119(8), 2368-2386.

[22] Gardner, L. and Ashraf, M. (2006). Structural design for non-linear metallic materials. Engineering Structures. 28(6), 926-934.

[23] EN 10088-1. (2005). Stainless steels – Part 1: List of stainless steels. CEN.

[24] EN 10088-2. (2005) Stainless steels – Part 2: Technical delivery conditions for sheet/plate and strip of corrosion resisting steels for general purposes. CEN.

[25] Cruise, R.B. and Gardner, L. (2008). Strength enhancements induced during cold forming of stainless steel sections. Journal of Constructional Steel Research. 64 (11), 1310-1316.

[26] Gardner, L., Talja, A. and Baddoo, N.R. (2006). Structural design of high-strength austenitic stainless steel. Thin-Walled Structures, 44(5), 517-528.

[27] Zhou, F. and Young, B. (2005). Tests of cold-formed stainless steel tubular flexural members. Thin-Walled Structures, 43(9), 1325-1337.

[28] Schafer, B.W. and Peköz, T. (1998). Computational modelling of cold-formed steel: characterizing geometric imperfections and residual stresses. Journal of Constructional Steel Research 47(3), 193-210.

[29] Cruise, R.B. and Gardner, L. (2006). Measurement and prediction of geometric imperfections in structural stainless steel members. Structural Engineering and Mechanics. 24(1), 63-89.

[30] Sherman DR. Tests of Circular Steel Tubes in Bending. J Struct Div, ASCE 1976;102:ST11.

[31] Jiao H. and Zhao X.L. (2004). Section slenderness limits of very high strength circular steel tubes in bending. Thin-Walled Structures. 42(9), 1257–71.

[32] ABAQUS. ABAQUS/Standard user's manual volumes I-III and ABAQUS CAE manual. Version 6.6. (Pawtucket, USA): Hibbitt, Karlsson & Sorensen, Inc; 2006

[33] Ramberg, W. and Osgood, W. R. (1943). Description of stress-strain curves by three parameters. Technical Note No 902, National Advisory Committee for Aeronautics Washington, D.C.

[34] Hill, H. N. (1944). Determination of stress-strain relations from the offset yield strength values. Technical Note No 927, National Advisory Committee for Aeronautics. Washington D.C.

[35] Mirambell, E. and Real, E. (2000). On the calculation of deflections in structural stainless steel beams: an experimental and numerical investigation. Journal of Constructional Steel Research. 54(1), 109-133.

[36] Rasmussen, K.J.R. (2003). Full-range stress-strain curves for stainless steel alloys. Journal of Constructional Steel Research. 59(1), 47-61.

[37] Gardner, L. and Nethercot, D.A. (2004). Experiments on stainless steel hollow sections - Part 1: Material and cross-sectional behaviour. Journal of Constructional Steel Research. 60(9), 1291-1318.

[38] Abdella, K. (2007). An explicit stress formulation for stainless steel applicable in tension and compression. Journal of Constructional Steel Research. 63(3), 326-331.

[39] Koltsakis, E.K. and Preftitsi, F.G. (2008). Numerical investigation of the plastic behaviour of short welded aluminium double-T beams. Engineering Structures 30 (7), 2022-2031.

[40] Rasmussen, K.J.R. and Hancock, G.J. (1993). Design of Cold-Formed Stainless Steel Tubular Members. I: Columns. Journal of Structural Engineering, ASCE. 119(8), 2349-2367.

[41] Cruise, R.B. and Gardner, L. (2008). Residual stress analysis of structural stainless steel sections. Journal of Constructional Steel Research. 64(3), 352-366.

[42] Gardner, L. and Nethercot D.A. (2004). Numerical Modelling of Stainless Steel Structural Components-A Consistent Approach. Journal of Structural Engineering, ASCE. 130(10), 1586-1601.

[43] Gardner, L. (2005). The use of stainless steel in structures. Progress in Structural Engineering and Materials. 7(2), 45-55.

[44] Sedlacek, G. and Feldmann, M. (1995). The b/t-ratios controlling the applicability of analysis models in Eurocode 3, Part 1.1. Background Document 5.09 for chapter 5 of Eurocode 3, Part 1.1, Aachen.

[45] Bild, S., Roik, K., Sedlacek, G., Stutzki, C. and Spangemacher, R. (1989). The b/t-ratios controlling the applicability of analysis models in Eurocode 3, Part 1.1. Background Document 5.02 for chapter 5 of Eurocode 3, Part 1.1, Aachen.

[46] Gerard G and Becker H. (1957). Handbook of structural stability: Part III—Buckling of curved plates and shells. Technical note 3783. NACA.

[47] Lay MG, Galambos TV. (1965). Inelastic steel beams under uniform moment. Journal of the Structural Division, ASCE. 91(6), 67–93.

[48] Lay MG, Galambos TV. (1967). Inelastic beams under moment gradient. Journal of the Structural Division, ASCE. 93(1), 381–99.

[49] Kuhlmann, U. (1989). Definition of Flange Slenderness Limits on the Basis of Rotation Capacity Values. Journal of Constructional Steel Research. 14(1), 21-40.

[50] Ashraf, M., Gardner, L. and Nethercot, D. A. (2008). Structural stainless steel design: Resistance based on deformation capacity. Journal of Structural Engineering, ASCE. 134(3), 402-411.

[51] Gardner, L. and Theofanous, M. (2008). Discrete and continuous treatment of local buckling in stainless steel elements. Journal of Constructional Steel Research. 64(11), 1207-1216.

[52] Gardner, L. (2008). The continuous strength method. Proceeding of the Institution of Civil Engineers-Structures and Buildings. 161(3), 127-133.
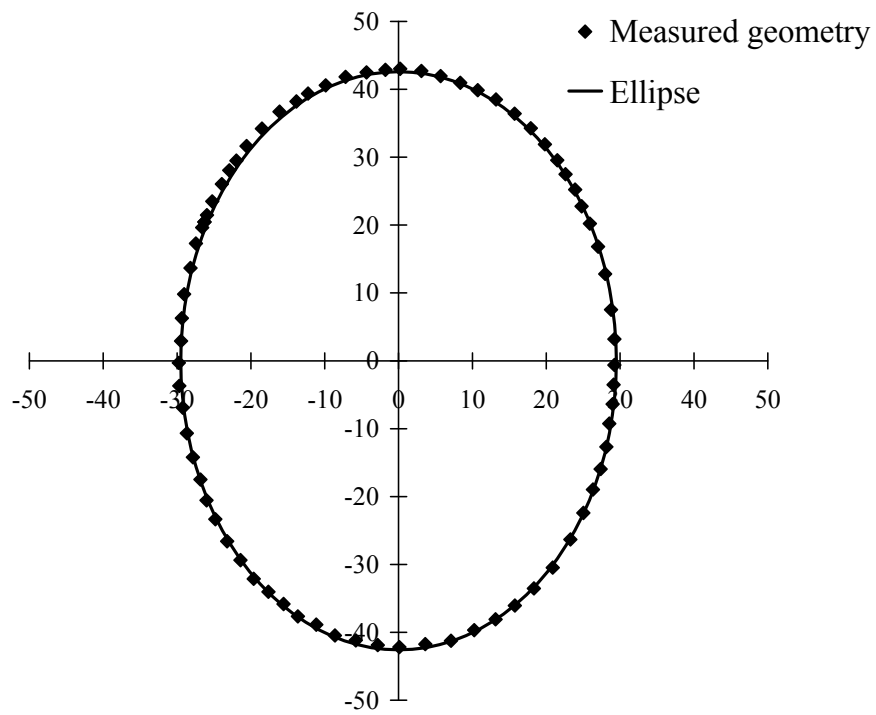
Fig. 1: Measured mid-surface geometry of oval section and elliptical representation
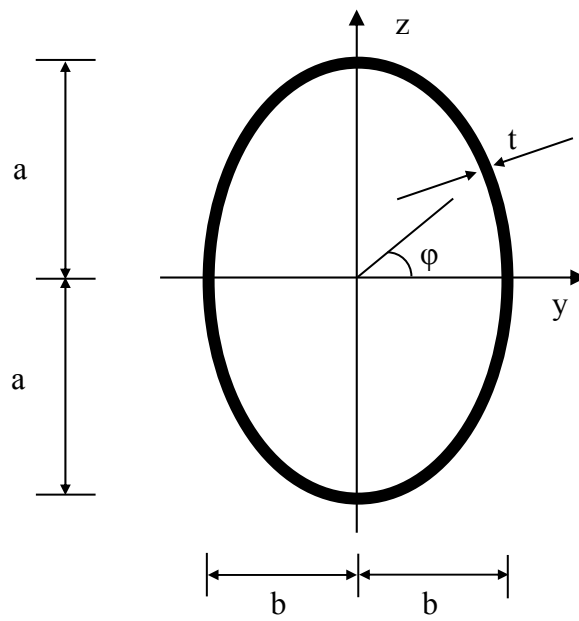
Fig. 2: Geometry and notation for oval hollow sections
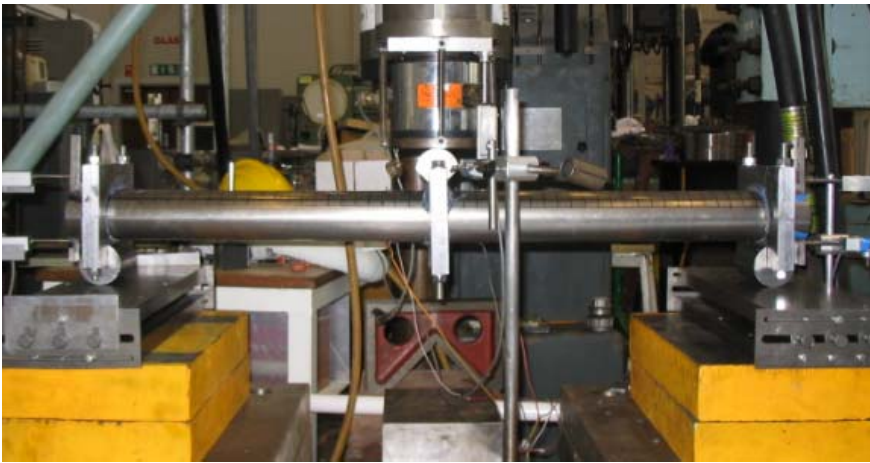
(a) Overall setup   (b) Support detail

Fig. 3: Three-point bending tests
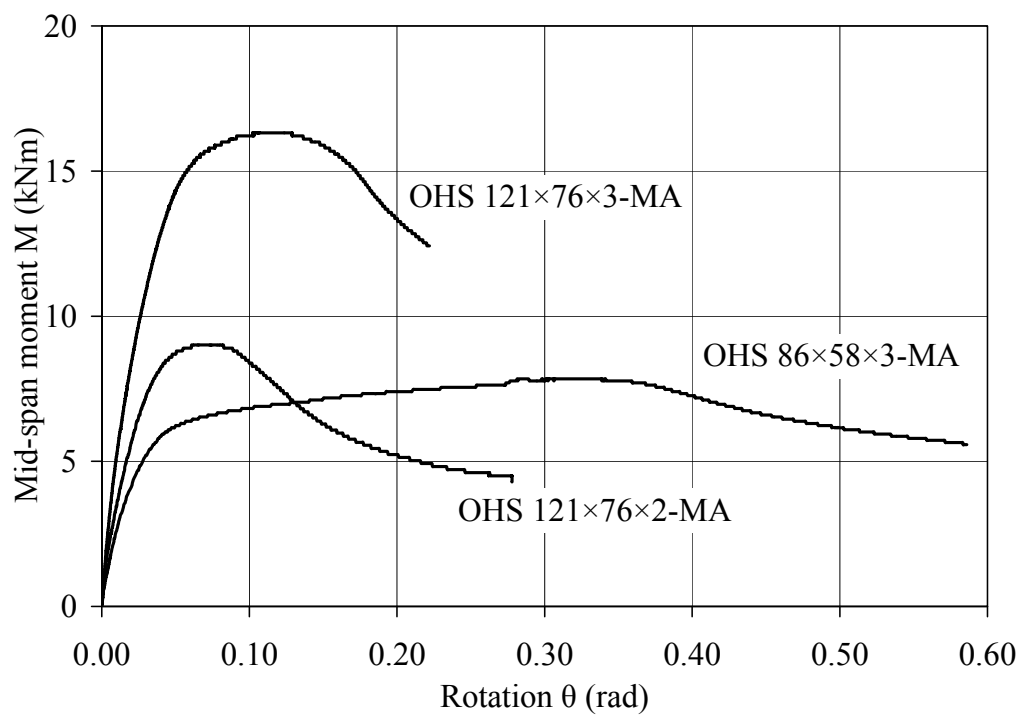
Fig. 4: Moment-rotation responses of specimens subjected to major axis bending
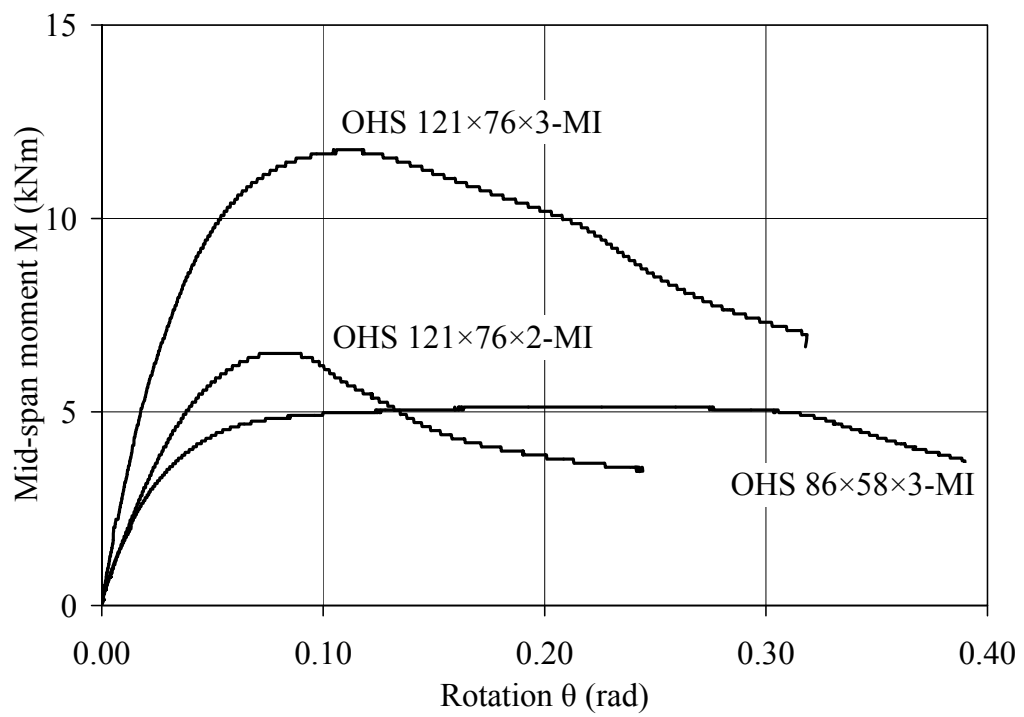
Fig. 5: Moment-rotation responses of specimens subjected to minor axis bending
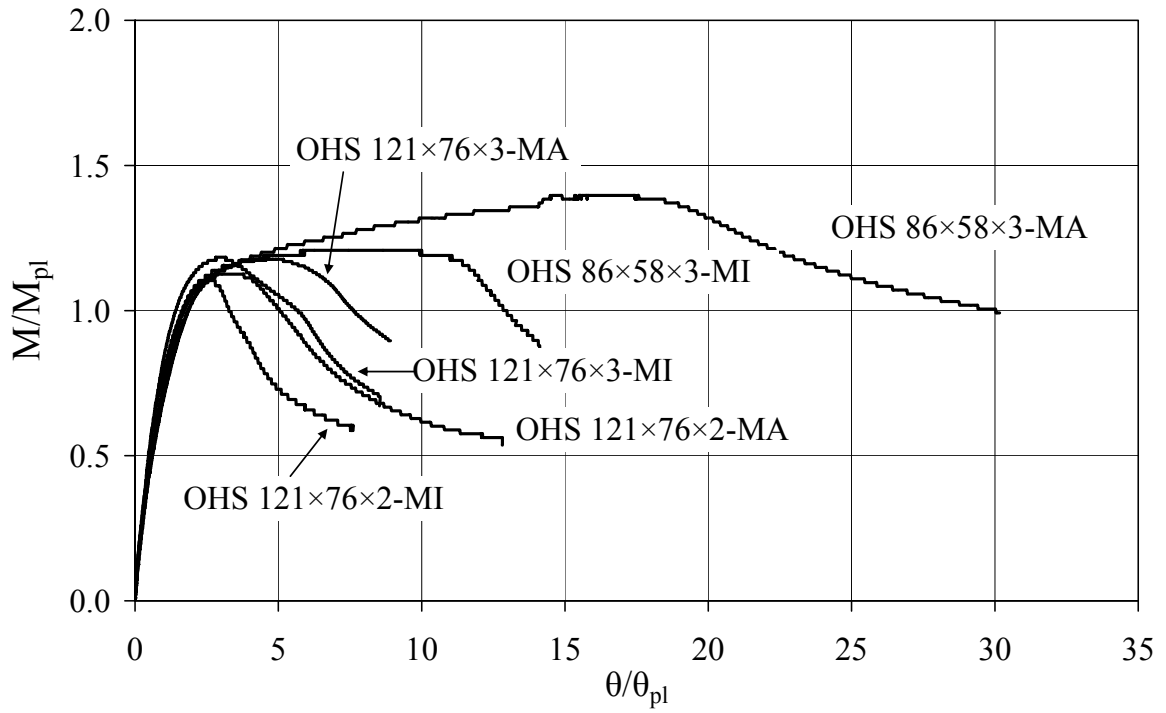
Fig. 6: Normalised moment-rotation curves for all specimens

a) OHS 86×58×3-MI

b) OHS 86×58×3-MA

c) OHS 121×76×3-MI

d) OHS 121×76×3-MA

e) OHS 121×76×2-MI

f) OHS 121×76×2-MA

Fig. 7: OHS specimen failiure modes
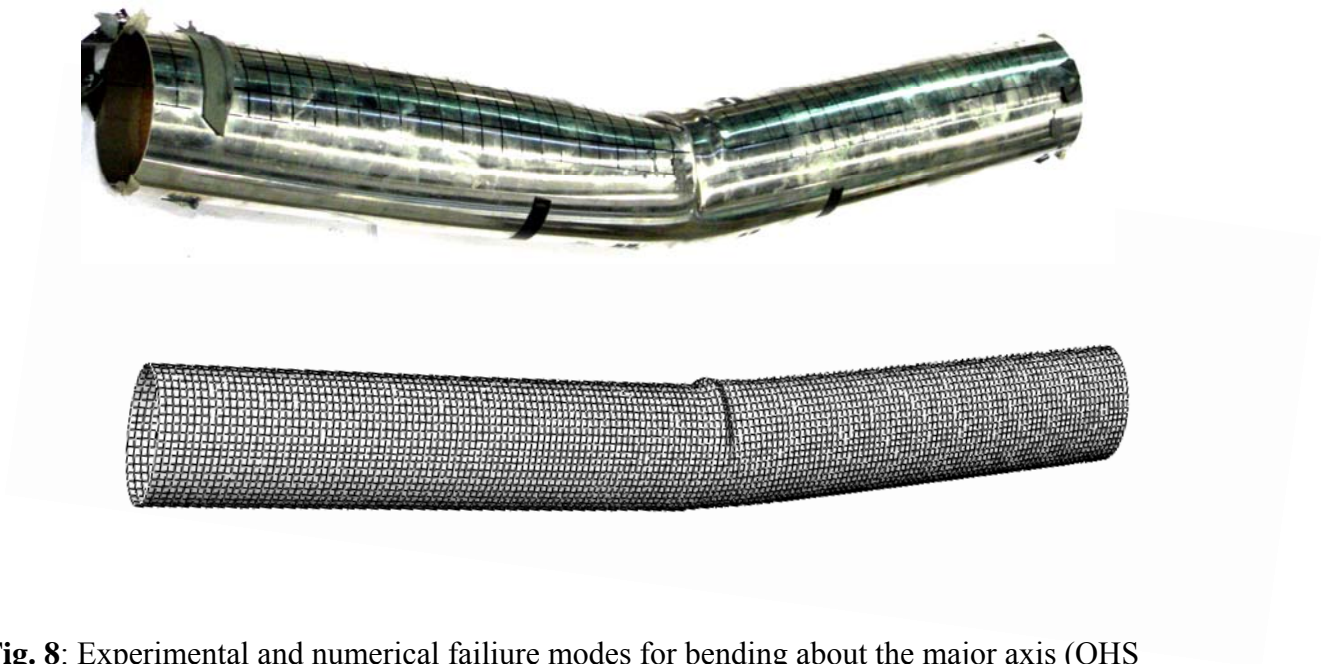
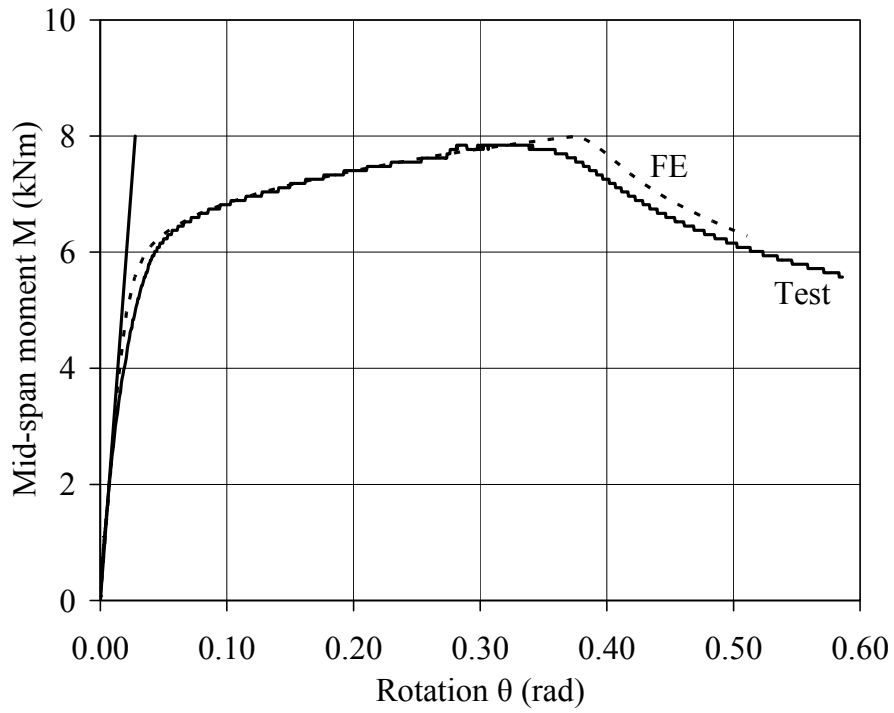**Fig. 8**: Experimental and numerical failiure modes for bending about the major axis (OHS 121×76×2-MA)
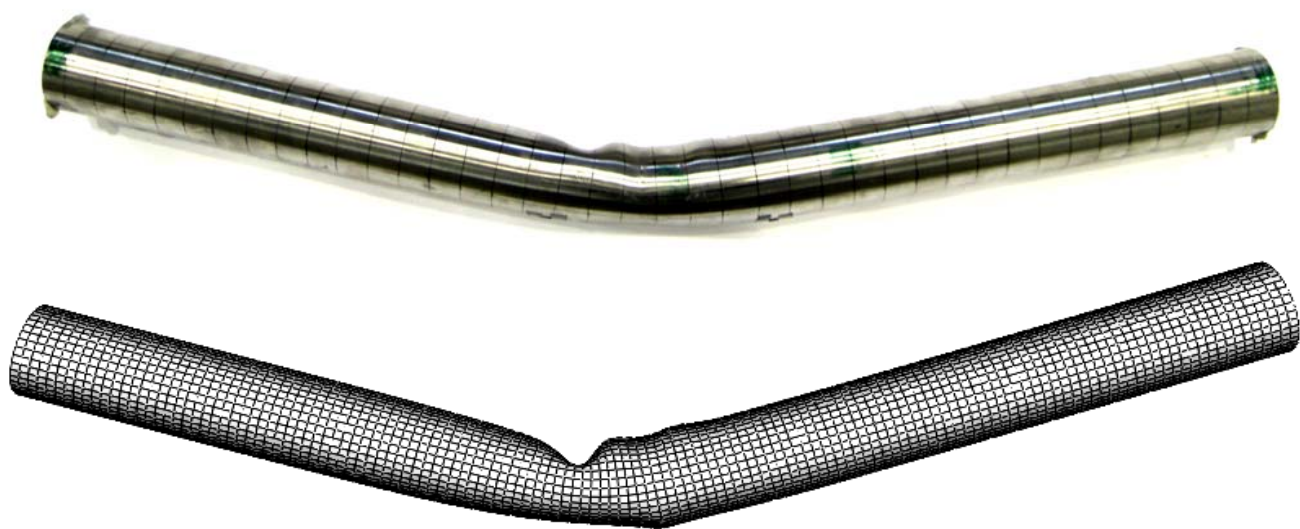
Fig. 9: Experimental and numerical failiure modes for bending about the minor axis (OHS 86×58×3-MI)
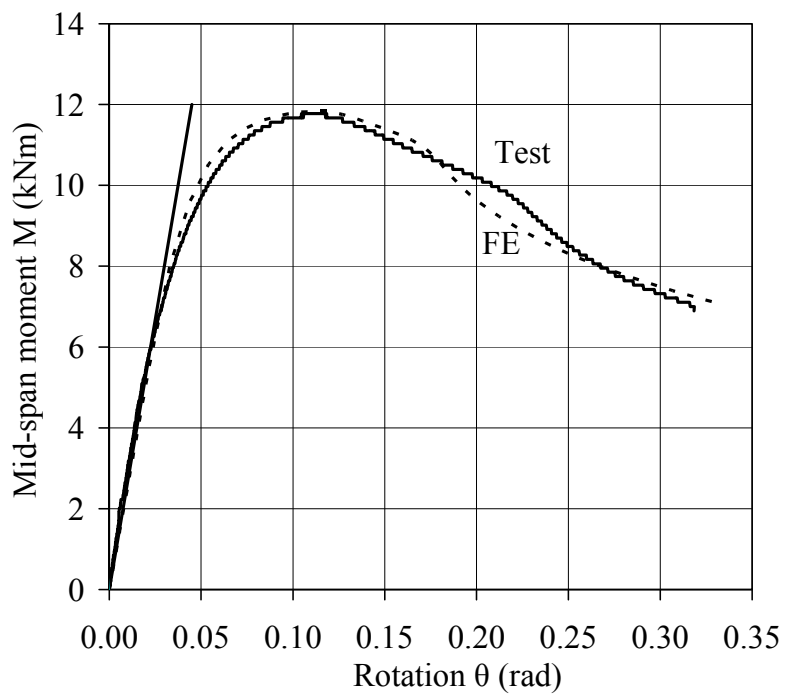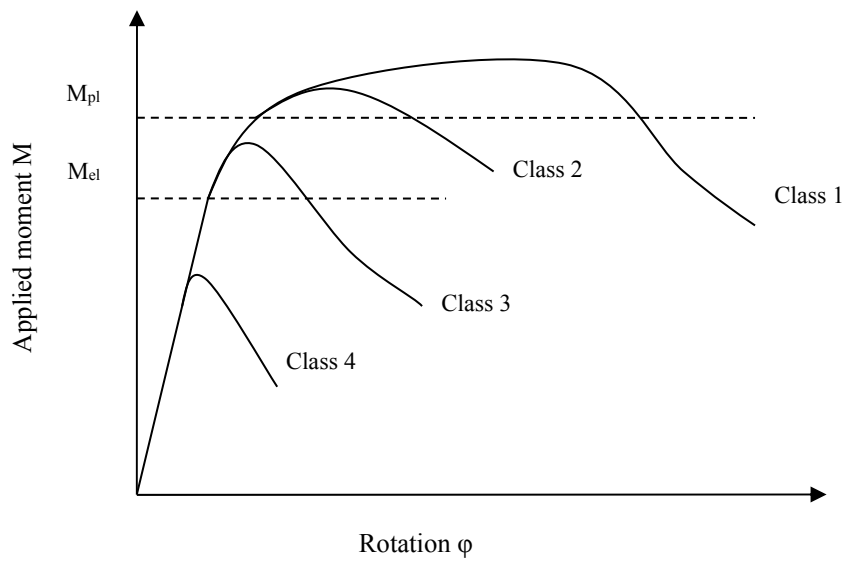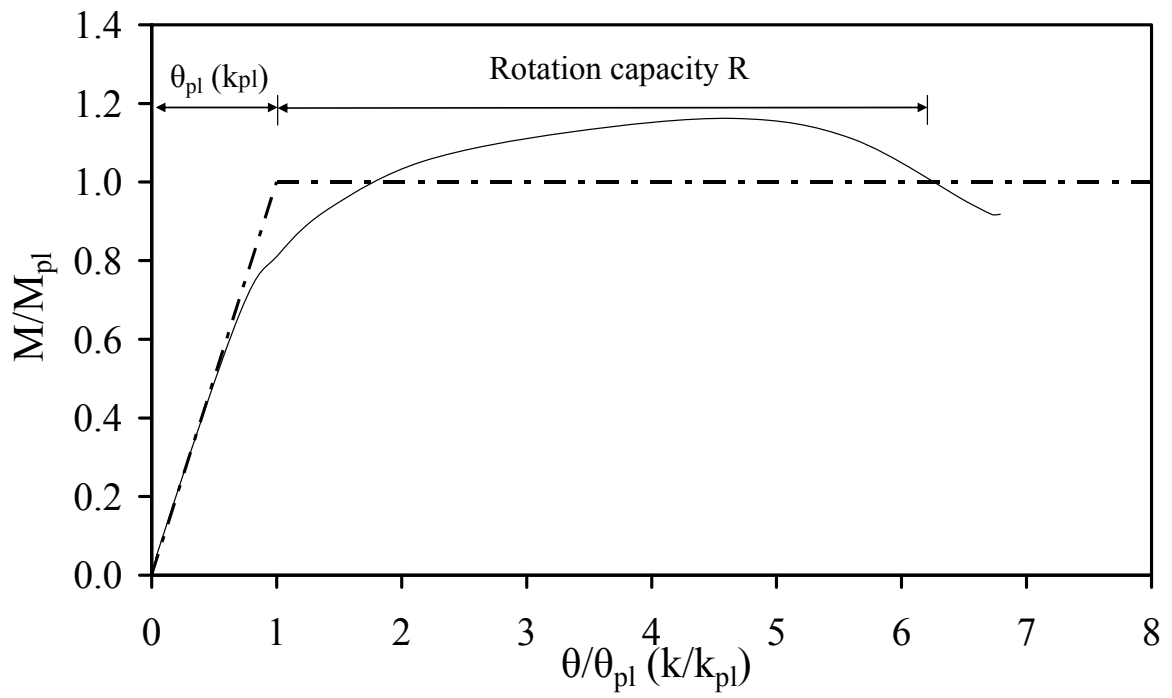
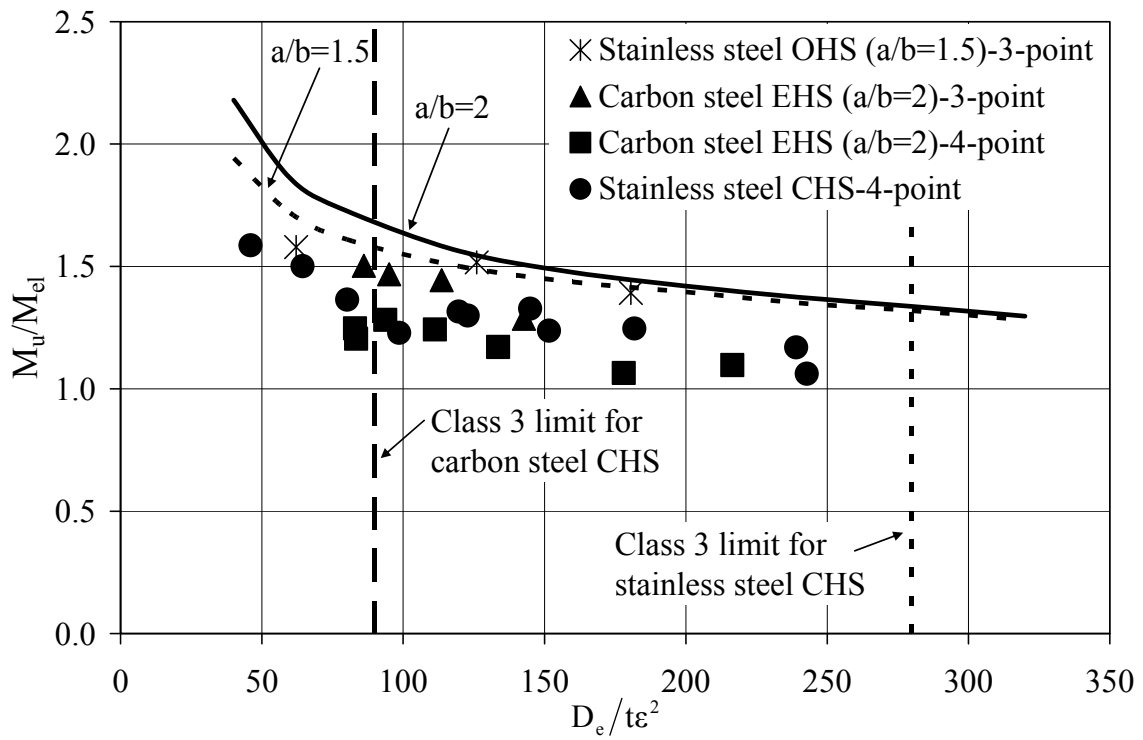**Fig. 10**: Experimental and numerical moment-rotation curves for OHS 121×76×3-MI specimen

Fig. 11: Experimental and numerical moment-rotation curves for OHS 86×58×3-MA specimen
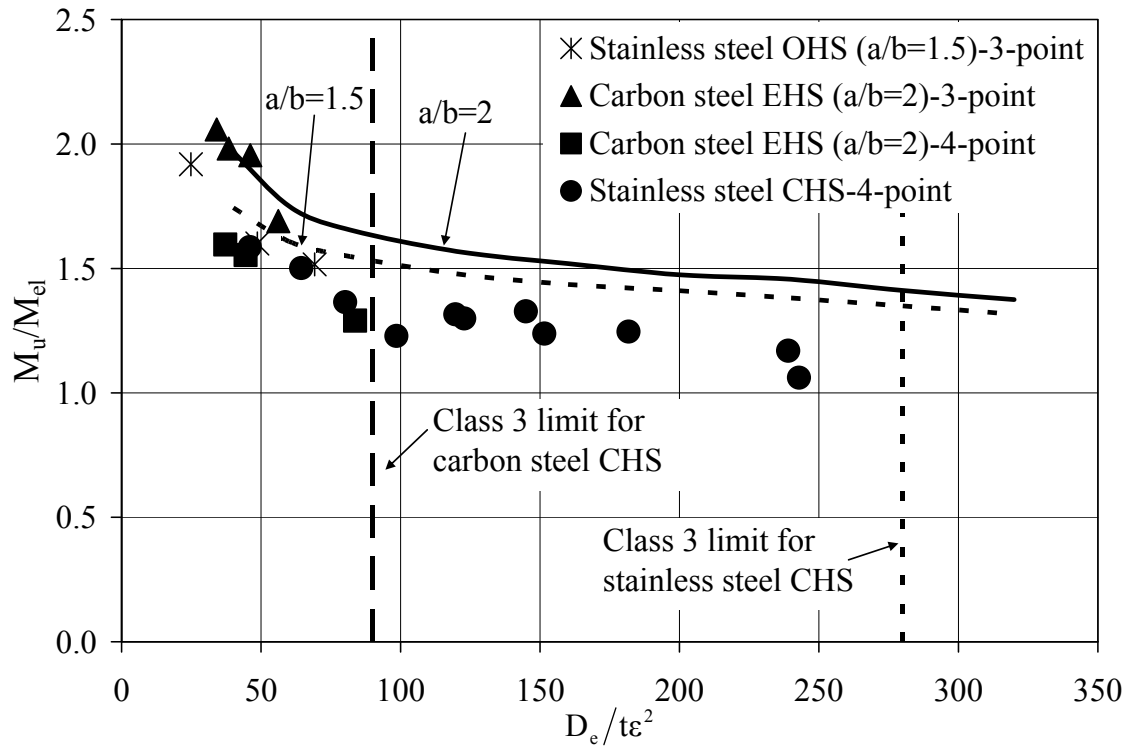
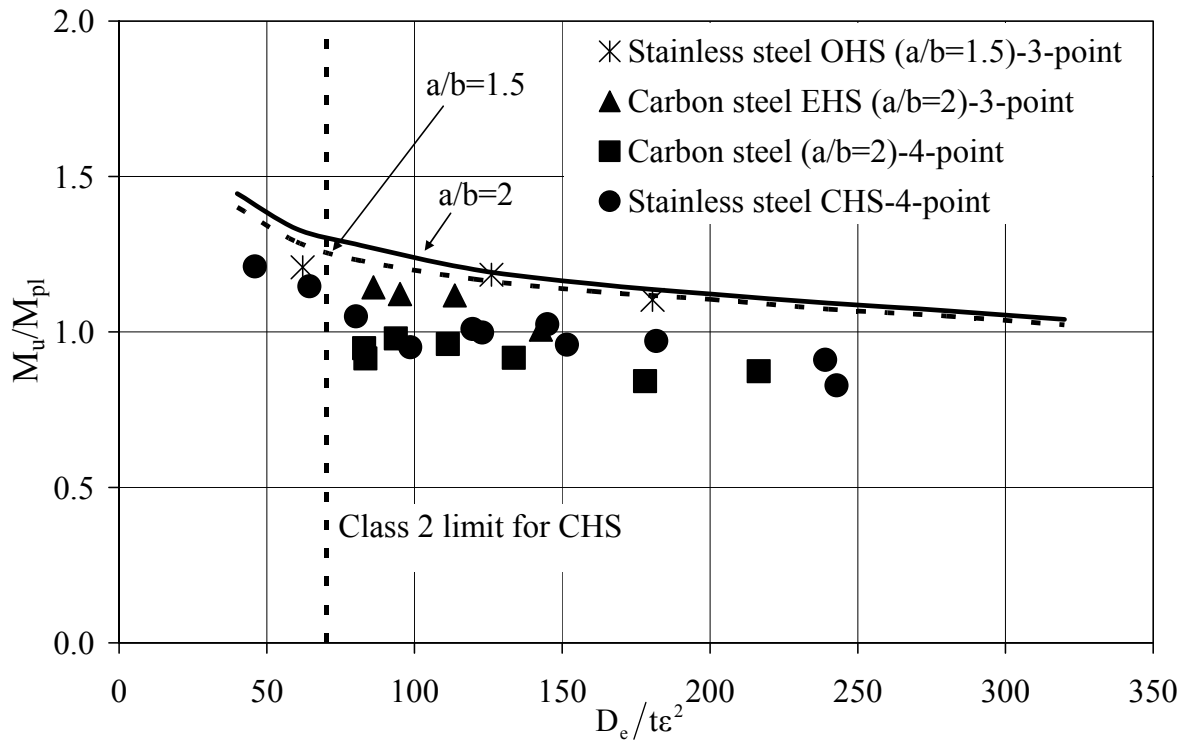**Fig. 12**: Four behavioural classes of cross-sections

Fig. 13: Definition of rotation capacity

Fig. 14: M_u/M_{el} versus cross-section slenderness for bending about the minor axis

Fig. 15: M_u/M_{el} versus cross-section slenderness for bending about the major axis
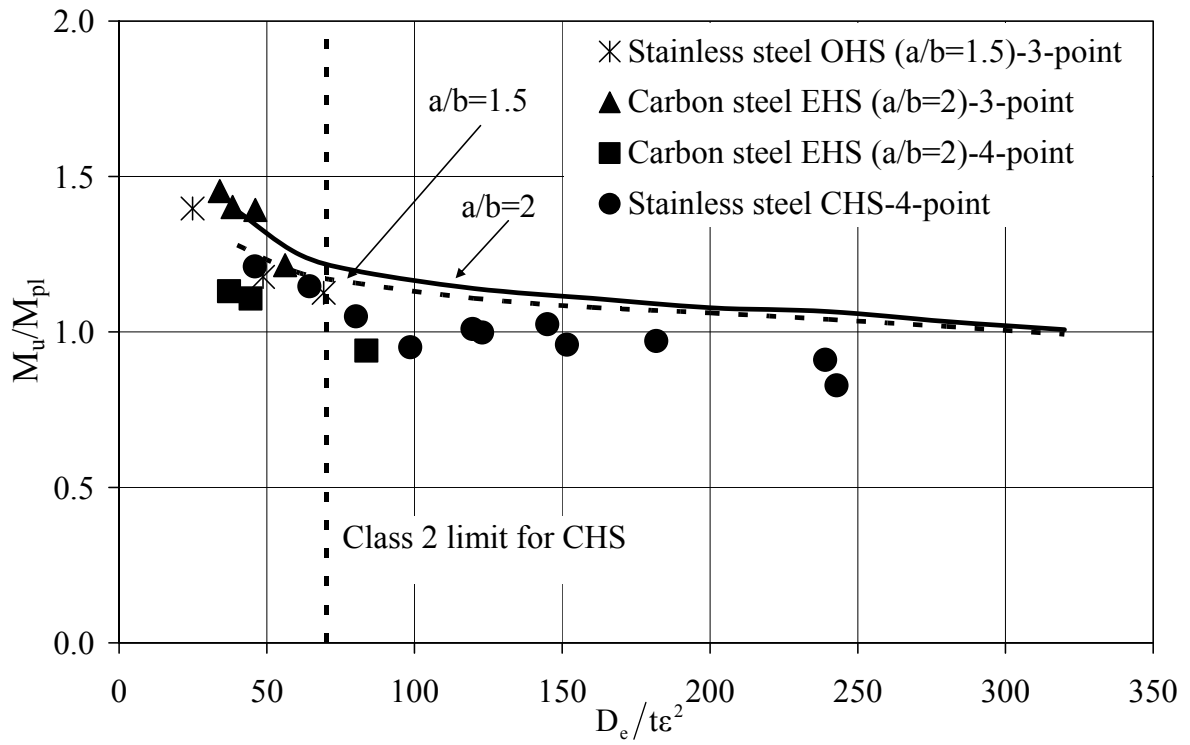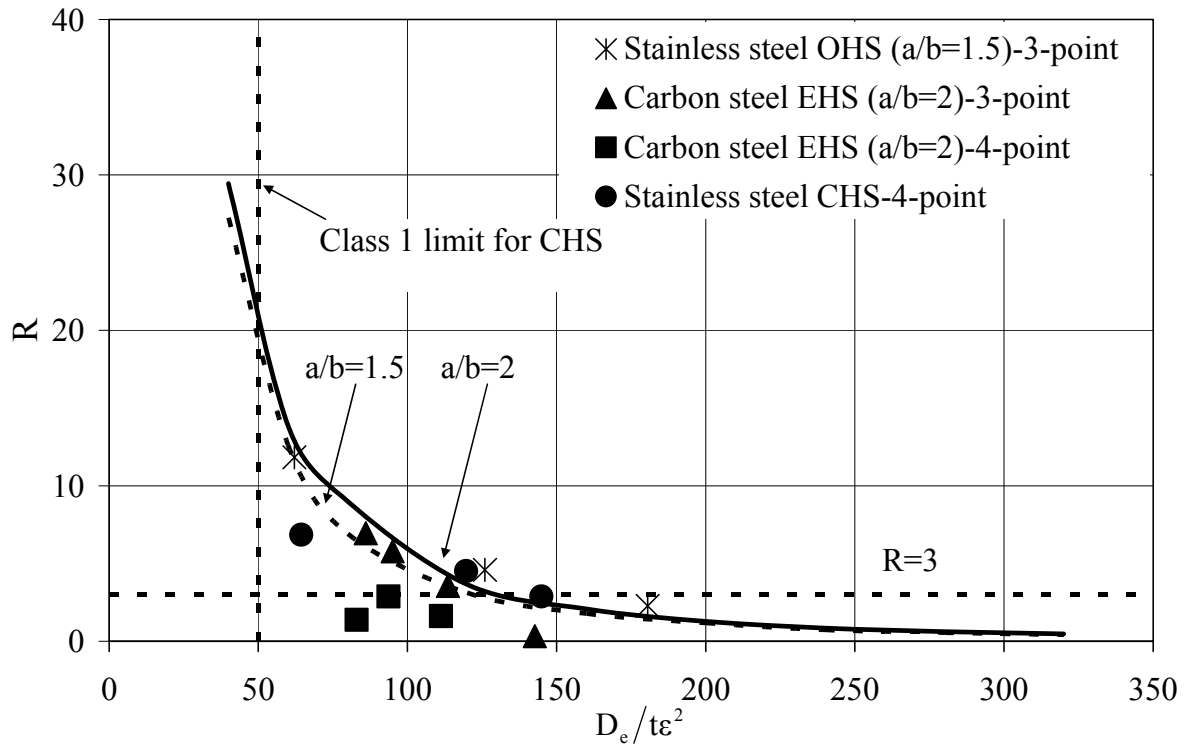
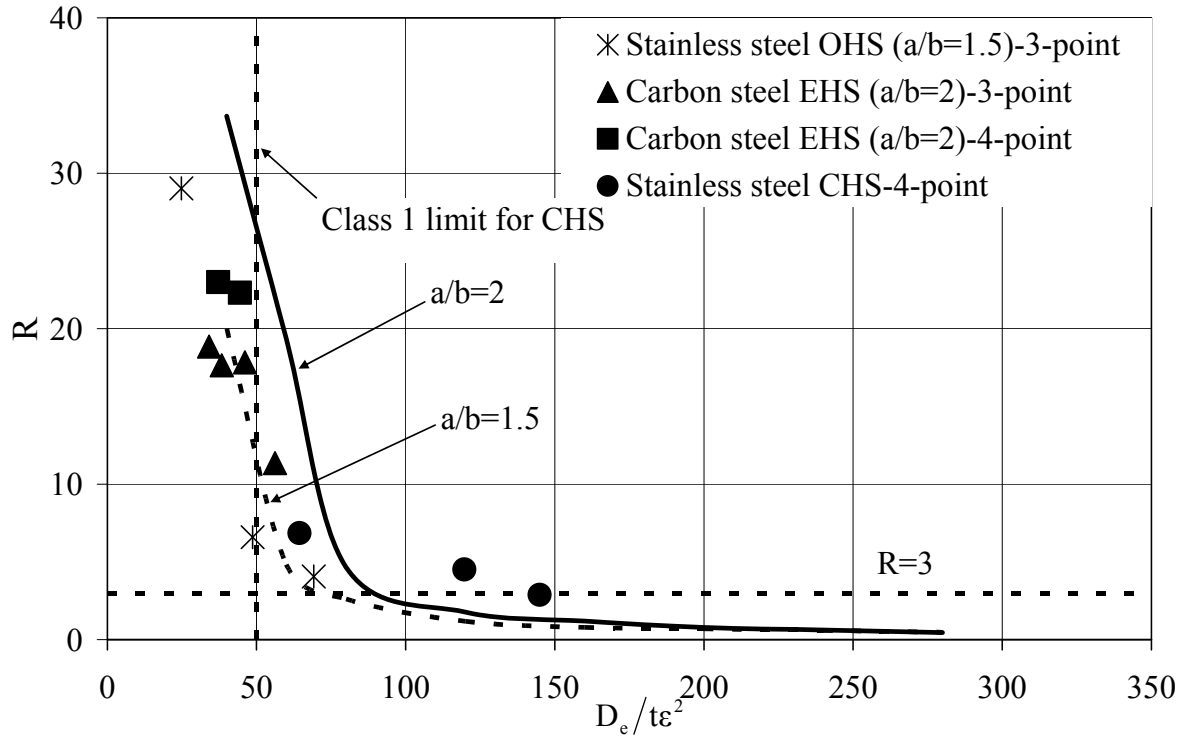**Fig. 16**: M_u/M_{pl} versus cross-section slenderness for bending about the minor axis

Fig. 17: M_u/M_{pl} versus cross-section slenderness for bending about the major axis

Fig. 18: Rotation capacity versus cross-section slenderness for bending about the minor axis

Fig. 19: Rotation capacity versus cross-section slenderness for bending about the major axis

Table 1 Measured material properties from tensile coupon tests

Coupon designation	E (N/mm²)	$\sigma_{0.2}$ (N/mm²)	$\sigma_{1.0}$ (N/mm²)	σ_u (N/mm²)	ε_f	Compound R-O coefficients	
						n	$n'_{0.2,1.0}$
OHS 121×76×2 - TC1	193900	380	426	676	0.61	7.8	2.9
OHS 121×76×2 - TC2	193300	377	419	672	0.60	8.9	2.9
OHS 121×76×3 - TC1	194100	420	460	578	0.58	9.7	4.0
OHS 121×76×3 - TC2	190400	428	467	583	0.58	8.2	4.0
OHS 86×58×3 - TC1	194500	339	368	586	0.62	14.0	1.8
OHS 86×58×3 - TC2	194500	331	349	597	0.62	13.5	1.3

Table 2 Measured material properties from stub column tests

Coupon designation	E (N/mm^2)	$\sigma_{0.2}$ (N/mm^2)	$\sigma_{1.0}$ (N/mm^2)	Compound R-O coefficients	
				n	n'$_{0.2,1.0}$
OHS 121×76×2 - SC1	185000	380	426	7.9	4.1
OHS 121×76×2 - SC2	189000	380	426	8.3	4.1
OHS 121×76×3 - SC1	176800	444	492	10.1	4.2
OHS 121×76×3 - SC2	176650	438	489	8.3	4.1
OHS 86×58×3 - SC1	178000	317	361	10.9	4.1
OHS 86×58×3 - SC2	182000	318	360	9.1	4.1

Table 3 Mean measured dimensions of bending specimens

Beam specimen designation	Axis of bending	Larger outer diameter 2a (mm)	Smaller outer diameter 2b (mm)	Thickness t (mm)	Length between supports L (mm)	Elastic section modulus W_{el} (mm^3)	Plastic section modulus W_{pl} (mm^3)	Measured maximum local imperfection w_0 (mm)
OHS 121×76×2 - MI	Minor	123.82	77.27	1.92	1006	12361	15596	0.42
OHS 121×76×2 - MA	Major	121.79	78.44	1.91	1003	15689	21134	0.38
OHS 121×76×3 - MI	Minor	121.79	77.08	3.01	1016	18312	23458	0.39
OHS 121×76×3 - MA	Major	121.35	78.74	3.03	1008	24049	32697	0.19
OHS 86×58×3 - MI	Minor	85.68	57.21	3.18	701	9697	12676	0.12
OHS 86×58×3 - MA	Major	85.47	57.17	3.17	702	12203	16760	0.12

Table 4 Summary of test results from 3-point bending tests

Beam specimen designation	Axis of bending	Ultimate moment M_u (kNm)	M_u/M_{el}	M_u/M_{pl}	Rotation capacity R
OHS 121×76×2 - MI	Minor	6.51	1.39	1.10	2.28
OHS 121×76×2 - MA	Major	9.00	1.52	1.13	4.06
OHS 121×76×3 - MI	Minor	11.78	1.52	1.18	4.59
OHS 121×76×3 - MA	Major	16.32	1.60	1.18	6.58
OHS 86×58×3 - MI	Minor	5.13	1.58	1.21	11.84
OHS 86×58×3 - MA	Major	7.84	1.92	1.40	29.02

Table 5 Comparison of the in-plane bending test results with FE results for varying imperfection amplitudes

Beam specimen designation	t/10		t/100		no imperfection		w_0	
	FE M_u/ Test M_u	FE R/ Test R	FE M_u/ Test M_u	FE R/ Test R	FE M_u/ Test M_u	FE R/ Test R	FE M_u/ Test M_u	FE R/ Test R
OHS 121×76×2 - MI	0.99	0.61	1.01	0.83	1.01	1.45	0.96	0.41
OHS 121×76×2 - MA	1.04	0.84	1.05	1.18	1.05	1.20	1.01	0.63
OHS 121×76×3 - MI	1.00	0.91	1.00	0.86	1.00	1.36	1.00	0.88
OHS 121×76×3 - MA	1.05	1.40	1.06	1.43	1.06	1.50	1.05	1.61
OHS 86×58×3 - MI	1.02	0.85	1.04	1.06	1.04	1.65	1.03	0.99
OHS 86×58×3 - MA	1.02	1.01	1.05	1.13	1.05	1.15	1.03	1.03
Mean	1.02	0.94	1.04	1.08	1.04	1.38	1.01	0.92
COV	0.02	0.28	0.02	0.21	0.02	0.14	0.03	0.44